The effects of Fe and NH4Cl on silicon nitridation

X.M. Yi (xuemei_yi@nwsuaf.edu.cn)
Northwest A&F University: Northwest Agriculture and Forestry University https://orcid.org/0000-0002-5714-1520

Senjing Zhang
Northwest A&F University: Northwest Agriculture and Forestry University

Weijun Zhu
Northwest A&F University: Northwest Agriculture and Forestry University

Qingda Li
Northwest A&F University: Northwest Agriculture and Forestry University

Wenjie Zhang
Northwest A&F University: Northwest Agriculture and Forestry University

Songze Li
Northwest A&F University: Northwest Agriculture and Forestry University

Research Article

Keywords: silicon nitride, Fe powder, NH4Cl, growth mechanisms

Posted Date: October 2nd, 2020

DOI: https://doi.org/10.21203/rs.3.rs-84111/v1

Abstract

Silicon nitride (Si3N4) with a high α-phase content is in demand due to its higher thermal conductivity for use in heat dissipation bases for electronic devices. However, more needs to be understood about its fibrous growth, therefore, rich fibrous morphologies were synthesized with the assistance of Fe powder and NH4Cl. The effects of these additives on the phase content and fiber morphologies of the products were investigated The results illustrate that the Si3N4 products possess upper and lower layers and that when the Fe powder content is 4 wt% and NH4Cl content is 5 wt%, the Si3N4 fibers have smooth surfaces, uniform diameters, and no floating particles. Moreover, the maximum α-Si3N4 content reached 94.8 wt%, demonstrating an increase in this phase. The double mechanisms of vapor-liquid-solid and vapor-solid are presented as the growth mechanism at the fiber.

1. Introduction

As a traditional structural material, silicon nitride (Si_3N_4) ceramics have been widely used in the machinery, automobile, space, and manufacturing industries due to their superior properties, such as high hardness and fracture toughness, good oxidation resistance, and corrosion resistance [1–3]. In recent years, Si_3N_4 ceramics have been used as heat dissipation base materials for electronic devices to provide good thermal conductivity and electrical insulation, along with good mechanical reliability [4]. To provide excellent thermal dissipation properties for substrate materials, many researchers have devoted themselves to improving the thermal conductivity of Si_3N_4 ceramics [5–8]. It is well known that, Si_3N_4 exists in two crystal structures at high temperatures: α and β. Si_3N_4 with a high α-phase content is significantly more effective in increasing the thermal conductivity and thus heat dissipation of the substrate material.

At present, the synthesis methods for Si_3N_4 include imide decomposition, carbothermal reduction, direct nitridation, the sol-gel method, and chemical vapor deposition. However, chemical vapor deposition and the sol-gel processes are complex, expensive, and unfriendly to the environment, and carbothermal reduction tends to introduce carbon powder into the final product. In contrast, direct nitridation at high temperatures with high-purity Si and N_2 to synthesize Si_3N_4 provides a method with low costs and high efficiency [9, 10]. In addition, through direct nitridation, the β phase was easily controlled by converting of α-phase at high temperatures [11]. Therefore, to obtain sintered Si_3N_4 powder with a high α-phase content, it is important to closely regulate production process.

According to relevant research, the addition of NaCl, NH_4Cl, KCl, and other molten salts into the raw reactants could effectively reduce the adiabatic temperature and stabilize the sintering reaction [12–14]. Additionally, previous research on the direct nitridation of Si_3N_4 has shown that the preparation of Si_3N_4 with high fibers content was beneficial to the thermal conductivity of Si_3N_4 ceramics owing to their low atomic mass, strong interatomic bonding, high modulus, small dielectric constant, high single crystal purity and fewer internal defects in the lattice [15–17]. The challenge of creating this structure is usually

solved by a combination of metallic addition and seeding. Adding Fe powder to the reactants could cause Si_3N_4 to generate a fibrous morphology, which strengthens the mechanical reliability of the material [18, 19].

Recently, some progress has been made in molten salt research to reduce the reaction temperature and change the morphology of products [20, 21]. Nevertheless, the mechanisms by which metals and molten salts are added to the reaction system and form Si_3N_4 fibers are still unclear. Hence, the purpose of this research is to prepare Si_3N_4 powers with a high α-phase and fibrous morphologies by direct nitridation with metal and molten salt additives of Fe powder and NH_4Cl, and to clarify the formation mechanism of Si_3N_4 fibers form the morphology of the final synthesized product.

2. Experimental

Si (purity > 99.99 wt%, 300 mesh, Adamas Reagent Co. Ltd., Shanghai) was used as the matrix, high-purity N_2 (purity > 99.999%) was used as nitrogen source. Meanwhile, NH_4Cl (purity ≥ 99.5 wt%, Guangzhou Jinhuada Chemical Reagent Co. Ltd.) and Fe powders (purity > 99 wt%, 100 mesh, Tianjin Beilianjingxi Chemical Reagent Co. Ltd.) were added to the reaction system as additives. The compositions of the samples are listed in Table 1, where F and, N represent Fe and NH_4Cl, respectively.

Table 1 Initial raw material composition mass ratio.

Sample (F: Fe; NH_4Cl: N)	Si (wt %)	Fe (wt %)	NH_4Cl (wt %)
F2N3	95	2	3
F3N3	94	3	3
F4N3	93	4	3
F5N3	92	5	3
F6N3	91	6	3
F4N1	95	4	1
F4N2	94	4	2
F4N4	92	4	4
F4N5	91	4	5

Figure 1 shows the experimental procedure. A planetary ball mill was used to dry mix the raw powder for 0.5 h at 1200 rpm, with a ball to raw material mass ratio of 5:1, using zirconium oxide balls with diameters of ϕ5 mm. Fifteen grams of the mixed powder sample was loosely loaded into an elliptical alumina crucible and placed in the center of the electric furnace for heat treatment, Through which 1 MPa of N_2 was continuously passed after achieving a vacuum. The furnace was heated from room

temperature to 1250–1550 °C for 4 h, then cooled to room temperature in the air. The samples were taken out and then ball milling. The phases of the ground products were characterized by X-ray diffraction (XRD, D8 ADVANCE, Bruker, Germany), and the microstructures were observed by scanning electron microscopy (SEM, Magellan 400, FEI, USA).

3. Results And Discussion

Figure 2 shows the XRD patterns obtained from the F4N3 sample after the synthesis of Si_3N_4 at different temperatures. α-Si_3N_4 and β-Si_3N_4 began to be produced at 1250 °C, and by the end the α-Si_3N_4 content was 39.2 wt%, but the product still contained residual 48.2 wt% Si powder. The α-Si_3N_4 content increased from 75.2 wt% to 88.5 wt% when the temperature increased from 1350 °C to 1450 °C, and the Si powder was fully reacted. Moreover, further increasing the temperature to 1550 °C reduced the content of α-Si_3N_4 to 54.9 wt%. The α-phase content was estimated from the intensity of the XRD peak. Therefore, as the temperature increased, the content of Si_3N_4 first increased and then decreased. Significantly, the content of α-Si_3N_4 increased rapidly at 1450 °C.

To analyze the effect of temperature on the synthesis of Si_3N_4 content, the calcination process of the product at different temperatures is shown in Fig. 1. The calcination profile of the product at 1250 °C revealed that the appearance structure of the product can be divided into the three layers. As we all know, Si and N_2 were reacted directly to obtain Si_3N_4 at 1300–1400 °C. However, according to reaction schemes (1)-(7), shown in Table 2, adding NH_4Cl to the raw materials effectively reduce the nitridation temperature of Si powder and produced α- and β-Si_3N_4 at 1250 °C. Further, when the temperature was above 1350 °C, the product images showed two layers. Thus, it is obvious that the appearance structure of product was related to the temperature, which is discussed in detail later.

Table 2
Seven potential reaction schemes present in this study

Chemical reaction schemes at different temperatures	
$NH_4Cl\ (s) \rightarrow NH_3\ (g) + HCl\ (g)$	T > 368 °C (1)
$Si\ (s) + 4HCl\ (g) \rightarrow SiCl_4\ (g) + 2H_2\ (g)$	T > 400 °C (2)
$3SiCl_4\ (g) + 4NH_3\ (g) \rightarrow Si_3N_4\ (s) + 12HCl\ (g)$	T > 400 °C (3)
$SiCl_4\ (g) + 2NH_3\ (g) \rightarrow Si(NH)_2 + 4HCl\ (g)$	T > 400 °C (4)
$3Si(NH)_2 \rightarrow Si_3N_4\ (amorph) + 2NH_3\ (g)$	T > 800 °C (5)
$Si_3N_4\ (amorph) \rightarrow \alpha\text{-}Si_3N_4$	T > 1200 °C (6)
$\alpha\text{-}Si_3N_4 \rightarrow \beta\text{-}Si_3N_4$	T > 1200 °C (7)
$Fe\ (s) + 2NH_4Cl\ (s) \rightarrow 2NH_3\ (g) + FeCl_2\ (s) + H_2\ (g)$	T > 204 °C (8)
$Fe\ (s) + HCl\ (g) \rightarrow FeCl_2\ (s) + H_2\ (g)$	T > 946 °C (9)
$FeCl_2\ (s) \rightarrow FeCl_2\ (g)$	T > 1023 °C (10)

Figure 3 shows the XRD patterns of Si_3N_4 obtained from the F2N3, F3N3, F4N3, F5N3 and F6N3 samples prepared for 4 h at 1450 °C. The XRD results indicate that the main substance in the products were α- and β-Si_3N_4 without any impurities. It can be seen that the α-Si_3N_4 content increased from 78.3 wt% to 94.8 wt%, meanwhile the β-Si_3N_4 content gradually decreased when the amount of Fe powder content increasing from 2 to 5 wt%. However, when the Fe powder content increased to 6 wt%, the α-Si_3N_4 content decreased and the β-Si_3N_4 content rapidly increased. This implies that the Fe powder content has an important effect on both the α- and β-Si_3N_4 content in the products.

According to analysis of reaction schemes (8)-(9) in Table 2, it is obvious that Fe powder plays an important role in the synthesis of Si_3N_4. When the temperature was above 204 °C, a small amount of Fe powder reacted with NH_4Cl to generate solid $FeCl_2$, gas NH_3, and H_2, which promoted reactions (3)-(5), and increased the generation of amorphous Si_3N_4. The amorphous Si_3N_4 then converted to α-Si_3N_4 and β-Si_3N_4 (reactions (6) and (7)). Further, increasing Fe powder content, some parts of the Fe powder reacted with HCl to generate solid $FeCl_2$ at temperatures above 946 °C. When the temperature continued to increase above 1023 °C, solid $FeCl_2$ powder began to sublimate, usually $FeCl_2$ melts at 946 °C and evaporates at 1023 °C. The phase change of $FeCl_2$ decreased the temperature of the reaction system, caused the formation of Si_3N_4 fibers at certain temperatures, meanwhile inhibited the α to β phase transition, which led to less β phase being formed [22]. Nevertheless, after increasing the Fe powder to 6 wt %, the excess Fe powder and Si formed a liquid Si-Fe alloy at high temperatures. The evaporation of

liquid Si-Fe alloy produced Si vapor, which reacted with N_2 to generate α-Si_3N_4 on the surface of the products, but the solid-liquid transition led to a large number of gaps and defects on the surface of the products, which caused N_2 to easily diffuse to the lower layer of the product, and promoted the formation of β-Si_3N_4 at high temperatures [23]. Therefore, the content of α-Si_3N_4 first increased and then decreased with an increasing amount of Fe powder.

Figure 4 shows the XRD patterns of products obtained from the F4N1, F4N2, F4N3, F4N4, and F4N5 samples prepared at 1450 °C for 4 h. Similar to the case of Fe powder, the α-Si_3N_4 content increased from 80.6 to 89.2 wt%, and the β-Si_3N_4 content gradually decreased with an increase in the NH_4Cl content from 1 to 4 wt%. However, when the NH_4Cl content was increased to 5 wt%, the content of α-Si_3N_4 decreased. This implied that the NH_4Cl content significantly affected the α-Si_3N_4 content.

According to the above analyses, Fe powder played an important role when adding a small amount of NH_4Cl, which was able to produce a large amount of β-Si_3N_4. However, as the NH_4Cl content increases, the heat of the reaction is absorbed by the NH_4Cl, and it decompose to NH_3 and HCl (reaction (1)), which further facilitates the generation of amorphous Si_3N_4, then α-Si_3N_4 (reactions (5) and (6)). Meanwhile, the latent heat of transition state $FeCl_2$ absorbs heat generated during nitridation, reducing the reaction system, and inhibiting the formation of β-Si_3N_4. Nevertheless, a large amount of gas generated by excess NH_4Cl can produce a fluffiness on the surface of the product, which destroys its surface structure, and increases the β-Si_3N_4 content. Hence, the content of α-Si_3N_4 first increases and then decreases with increasing NH_4Cl.

Figure 5 shows the SEM images of the Si_3N_4 products synthesized from F2N3 and F5N3 samples at 1450 °C for 4 h (U and L represent the upper and lower layers of product, respectively). Figure 5 (a) and (b) show that the upper layer morphologies of product are comprised of thin nanowires with rough surfaces, thick nanowires with smooth surfaces, and floating particles (circle 2 in Fig. 5 (b)). The average diameter of the thin nanowires was about 1 μm, and the average diameter of the thick nanowires was about 3 μm. The SEM images in Fig. 5 (a) indicate that the Si_3N_4 nanowires surface was rough. Figure 5 (b) shows that Si_3N_4 nanowires were straight with smooth surfaces, containing some floating particles. Figures 5 (c) and (d) show the lower layer morphologies of the products were loose and short rod-like nanowires, long needle-like nanowires, and blocky particles.

Figure 6 shows the SEM images of the Si_3N_4 products synthesized from the F4N1 and F4N5 samples at 1450 °C for 4 h (U and L represent the upper and lower layers of the product, respectively). Figures 6 (a) and (b) show that the upper layer morphologies are comprised of thin nanowires with smooth surfaces and some floating particles (circle 2 in Fig. 6 (a)). The average diameter of nanowires was about 1 μm, which was more uniform, compared to those in Figs. 5 (a) and (b). However, some of the floating particles were adsorbed on the surface of the nanowires. Figures 6 (c) and (d) show that the lower layer product morphologies contained short rod-like nanowires, long needle-like nanowires, and dense and blocky Si_3N_4.

Currently, it is generally accepted that the growth mechanism of nanowires includes the double-stage vapor-liquid-solid (VLS) and vapor-solid (VS) mechanisms at the tip. [24–26]. Figure 5 (b) 1 and Fig. 6 (b) 1 show that there were no traces of liquid generation at the nanowire tips, Hence, the nanowires may grow via a vapor-solid (VS) process. However, according to reactions 6, 9, and 10 and the melting and boiling points of the Si-Fe alloy and $FeCl_2$, nanowires should theoretically grow via the VLS mechanisms. Therefore, the formation mechanism of Si_3N_4 fiber may have two growth mechanisms.

The simplified growth models of the fibers are shown in Fig. 7. The fiber growth of the upper layer mainly depends on temperature. On the one hand, when the temperature is above 946 °C, a large amount of amorphous Si_3N_4 is produced (reaction (5)), meanwhile the solid $FeCl_2$ is transformed into a liquid, which is adhered onto the surface of the amorphous Si_3N_4. When the temperature increases above 1023 °C, amorphous Si_3N_4 gradually generates fibrous Si_3N_4 form liquid $FeCl_2$, and the $FeCl_2$ droplets gradually evaporate and disappear with temperature increases. On the other hand, when the temperature is above 1300 °C, the Si-Fe alloy produces Si vapor, which reacts with N_2 to nucleate and then grow into Si_3N_4, then the Fe droplets gradually evaporate and disappear at high temperatures. Moreover, at high temperatures, a small amount of Si vapor reacts directly with N_2 to generate Si_3N_4, which was then absorbed onto the fiber surface (circle 2 in Figs. 5 (b) and 6 (a)). It is clear that when the ratio of Fe powder and NH_4Cl in the raw material is low, the product mainly produces Si_3N_4 fibers with a rough surface and a small diameter. However, as the Fe powder content increases, the surface of the Si_3N_4 fiber becomes smoother, and the average diameter of the Si_3N_4 fiber gradually increases, and the amount and density of the floating particles gradually increases.

In addition, the product growth formed on the lower layer product includes fibers and stacked blocks, increasing the ratio of Fe powder to NH_4Cl, the number of long needle-like fibers, and the density of blocky structures, while decreasing the number of short rod-like fibers. There could be two reasons for this growth analysis of products in the lower layer. On the one hand, the fiber growth mechanism in the lower layer could be similar to the fiber growth mechanism in the upper layer, but because of the effect of the weight of $FeCl_2$ and Si-Fe droplets, most of the $FeCl_2$ and Si-Fe droplets are adsorbed on the surface of the Si powders, causing the Si on the surface to react with the N_2 adsorbed by the droplets to generate fibers, but the Fe powder and NH_4Cl produced gas to destroy the formation of nanowires during nitridation, thus forming short rod-like and long needle-like fibers. On the other hand, a small amount of Si powder particles in the lower layer could gradually react with N_2 and continuously stack to form a blocky structure.

4. Conclusions

Si_3N_4 with a high α phase content and rich fiber morphologies was synthesized via a direct nitridation method by adding Fe powder and NH_4Cl to the raw reactants, the following conclusions can be obtained.

(1) Si powder fully reacted when Fe powder and NH_4Cl were added at 1350 °C.

Additionally, at 1450 °C, it was found that the Fe powder content was 5 wt% and the NH_4Cl content was 3 wt%, the maximum α-Si_3N_4 content reached was 94.8 wt%.

(2) The obtained Si_3N_4 products possessed upper and lower layers. Where the upper layer products were composed of fibrous morphologies, while the lower layer of products mainly consisted of short rod-like fibers and blocky structures. The results show that when the Fe powder content was 4 wt% and the NH_4Cl content was 5 wt%, the Si_3N_4 possessed a smooth surface, uniform diameter, and no floating particles.

Si_3N_4 containing high α phase with different nanostructure morphologies can be synthesized through a direct nitriding method. However, the morphologies of the products at the upper and lower layers are greatly different. Therefore, the prepared Si_3N_4 with uniform fibrous morphologies is an urgent issue to be solved in future.

Declarations

Acknowledgments

This work was financially supported by Shaanxi Key R&D Program (No.2018GY-116). We gratefully acknowledge the Institute of Water-Saving Agriculture in Arid Areas of China (IWSA), the Life Science Research Core Services of Northwest A&F University for XRD analyses.

References

1. Kadin Y, Strobl S, Vieillard C, Wijnbergen P, Ocelik V (2017) In-situ observation of crack propagation in silicon nitride ceramics. Procedia Structural Integrity 7:307–314. https://doi.org/10.1016/j.prostr.2017.11.093
2. Xing H, Liu B, Sun J, Zou B (2017) Mechanical properties of Si_3N_4 ceramics from an in-situ synthesized a-Si_3N_4/β-Si_3N_4 composite powder. Ceram Int 43:2150–2154,. http://dx.doi.org/10.1016/j.ceramint.2016.10.196
3. Li S, Li Y, Xiao H, Li X, Wang Q, Tang M, Tu H, Huang J, Chen L, Yu Z (2018) Oxidation behavior of Si_3N_4 fibers derived from polycarbosilane. Corros Sci 136:9–17. https://doi.org/10.1016/j.corsci.2018.02.032
4. Zhou Y, Hyuga H, Kusano D, Yoshizawa Y, Ohji T, Hirao K (2018) Development of high-thermal-conductivity silicon nitride ceramics. J Asian Ceam Soc 3:221–229. http://dx.doi.org/10.1016/j.jascer.2015.03.003
5. Yin J, Yao D, Xia Y, Zuo K, Zeng Y (2014) Enhanced thermal conductivity of Cu matrix composites reinforced with Ag-coated β-Si_3N_4 whiskers. Materials Design 60:282–288. http://dx.doi.org/10.1016/j.matdes.2014.03.0470261-30

6. Takahashi T, Sado M, Sugimoto N, Tatami J, Iijima M, Inagaki S, Kubota Y, Yamamoto I, Tanaka S (2016) Fabrication of c-axis oriented Si_3N_4 ceramics using multilayered-graphene-coated β-Si_3N_4 seeds and their orientation in an innovative low magnetic field. Adv Powder Technol 27:2005–2011. http://dx.doi.org/10.1016/j.apt.2016.07.006
7. Lee HM, Lee EB, Kim DL, Kim DK, Comparative study of oxide and non-oxide additives in high thermal conductive and high strength Si_3N_4 ceramics. Ceramics International 42 (2016) 17466–17471, http://dx.doi.org/10.1016/j.ceramint.2016.08.051
8. Jia H, Li J, Rui N, Ye C, Ru H, Liu B, Y. E, and Li H (2018) Fabrication of β-Si_3N_4 with high thermal conductivity under ultra-high pressure. Ceram Int 44:23288–23292. https://doi.org/10.1016/j.ceramint.2018.09.030
9. Gundiah G, Madhav GV, Govindaraj A, Seikh MM, Rao CNR (2002) Synthesis and characterization of silicon carbide, silicon oxynitride and silicon nitride nanowires. J Mater Chem 12:1606–1611. https://doi.org/10.1039/B200161F
10. Ren H, Zhang L, Su K, Zeng Q, Cheng L (2015) Thermodynamic study on the chemical vapor deposition of silicon nitride from the $SiCl_4$–NH_3–H_2 system. Comput Theor Chem 1051:93–103. http://dx.doi.org/10.1016/j.comptc.2014.11.003
11. Chung YK, Koo JH, Kim SA, Chi EO, Hahn JH, Park C (2014) Optimization of reaction parameters for synthesis of amorphous silicon nitride powder by vapor phase reaction. Ceram Int 40:14563–14568. http://dx.doi.org/10.1016/j.ceramint.2014.06.040
12. Ding J, Zhu H, Li G, Deng C, Chai Z (2016) Catalyst-assisted synthesis of α-Si_3N_4 in molten salt. Ceram Int 42:2892–2898. http://dx.doi.org/10.1016/j.ceramint.2015.10.066
13. Liu X, Yi X, Guo R, Li Q, Nomura T (2017) Formation mechanisms of Si_3N_4 microstructures during silicon powder nitridation. Ceram Int 43:16773–16779. http://dx.doi.org/10.1016/j.ceramint.2017.09.072
14. Niu J, Suzuki S, Yi X, Akiyama T (2015) Fabrication of AlN particles and whiskers via salt-assisted combustion synthesis. Ceram Int 41:4438–4443. http://dx.doi.org/10.1016/j.ceramint.2017.09.072
15. Zhu X, Zhou Y, Hirao K (2006) Effects of processing method and additive composition on microstructure and thermal conductivity of Si_3N_4 ceramics. J Eur Ceram Soc 26:711–718. https://doi.org/10.1016/j.jeurceramsoc.2005.07.027
16. Kim J, Ko S, Kim H, Ko J, Lee J, Kim H, Park Y (2017) Effects of microstructure and intergranular glassy phases on thermal conductivity of silicon nitride. Ceram Int 43:5441–5449. http://dx.doi.org/10.1016/j.ceramint.2017.01.037
17. Liang H, Zeng Y, Zuo K, Xia Y, Yao D, Yin J, Mechanical properties and thermal conductivity of Si_3N_4 ceramics with YF_3 and MgO as sintering additives. Ceramics International 42 (2016) 15679–15686, http://dx.doi.org/10.1016/j.ceramint.2016.07.024
18. Ge Y, Sun S, Wang Q, Cui W, Zou Y, Xie Z, Chen K (2016) Effect of Fe-Contained Species on the Preparation of α-Si_3N_4 Fibers in Combustion Synthesis. J Am Ceram Soc 99:1464–1471.

https://doi.org/10.1111/jace.14134

19. Li B, Chen JH, Su JD, High Temperature Stability of Fe_{pure}-Si_3N_4 in Reducing Atmosphere. Advanced Materials Research 952 (2014) 11–15, https://doi.org/10.4028/www.scientific.net/AMR.952.11
20. Liu X, Guo R, Zhang S, Li Q, Saito G, Yi X, Nomura T (2018) Formation of Different Si_3N_4 Nanostructures by Salt-Assisted Nitridation. ACS Appl Mater Interfaces 10:11852–11861. https://doi.org/10.1021/acsami.7b16952
21. Yi X, Li Q, Suzuki S, Zhang S, Nomura T, Akiyama T (2019) Combustion synthesis of α-Si_3N_4 assisted by molten salt additives. Ceram Int 45:10021–10027. https://doi.org/10.1016/j.ceramint.2019.02.046
22. Huo K, Ma Y, Hu Y, Fu J, Lu B, Lu Y, Hu Z, Chen Y (2005) Synthesis of single-crystalline alpha-Si_3N_4 nanobelts by extended vapour-liquid-solid growth. Nanotechnology 16:2282–2287. DOI:10.1088/0957-4484/16/10/050
23. Kusano D, Noda Y, Shibasaki H, Hyuga H, Zhou Y, Hirao K (2013) Effects of Impurity Iron Content on Characteristics of Sintered Reaction-Bonded Silicon Nitride. Int J Appl Ceram Technol 10:690–700. https://doi.org/10.1111/j.1744-7402.2012.02767.x
24. Huang J, Huang Z, Yi S, Liu Y, Fang M, Zhang S (2013) Fe-catalyzed growth of one-dimensional α-Si_3N_4 nanostructures and their cathodoluminescence properties. Sci Rep 3:1–7. DOI:10.1038/srep03504
25. Hu P, Dong S, Fang C, Cheng Y, Sun B, Chen G, Ultra-long Si_3N_4 nanobelts prepared by nanosilicon, nanosilica and graphite. Materials Science in Semiconductor Processing 56 (2016) 189–195, http://dx.doi.org/10.1016/j.mssp.2016.08.020
26. Du H, Zhang W, Li Y (2014) Effects of growth parameters on the yield and morphology of Si_3N_4 microcoils prepared by chemical vapor deposition. Mater Res Bull 50:57–62. http://dx.doi.org/10.1016/j.materresbull.2013.09.023

Figures

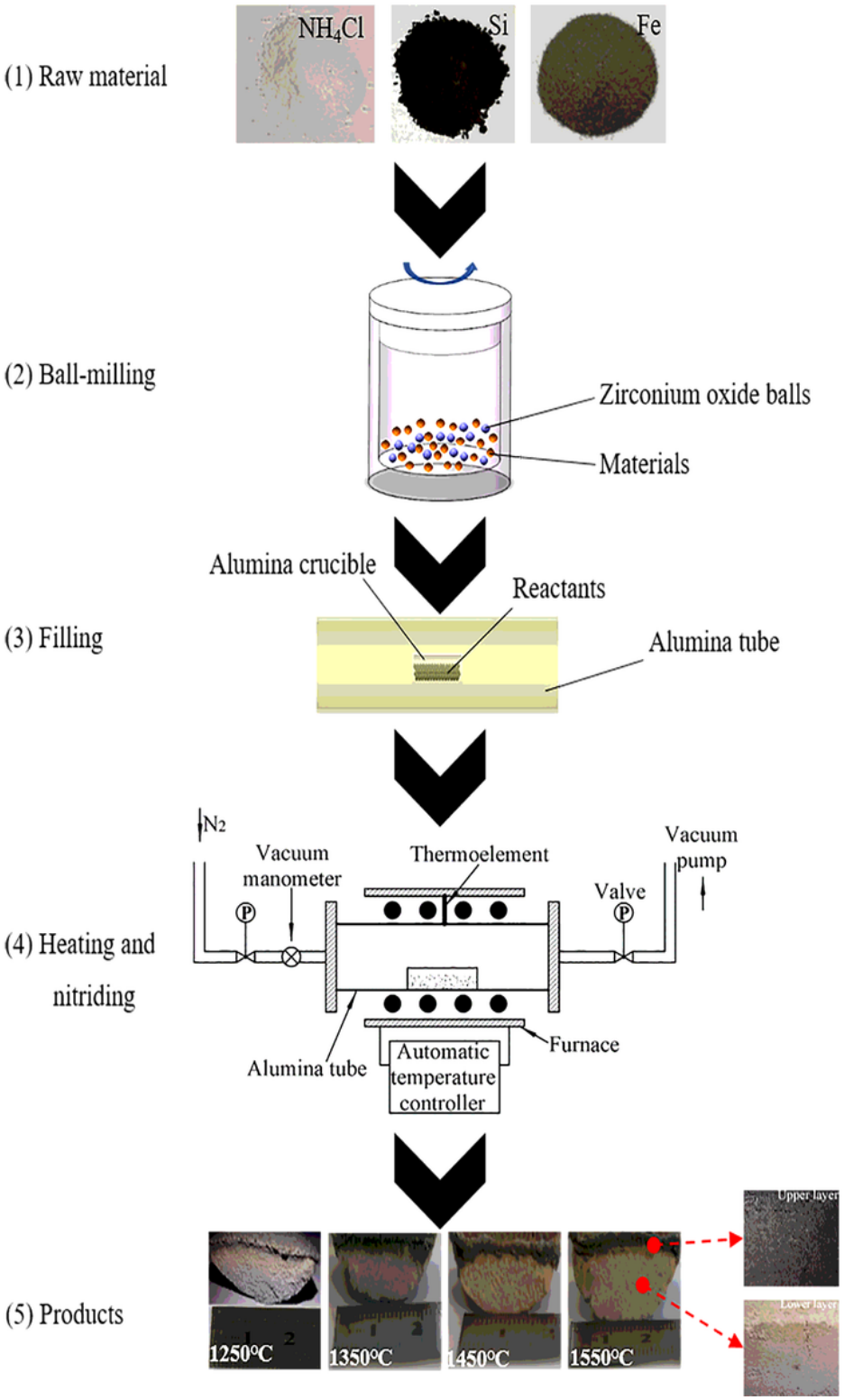

Figure 1

Experimental schematic diagram for direct nitridation.

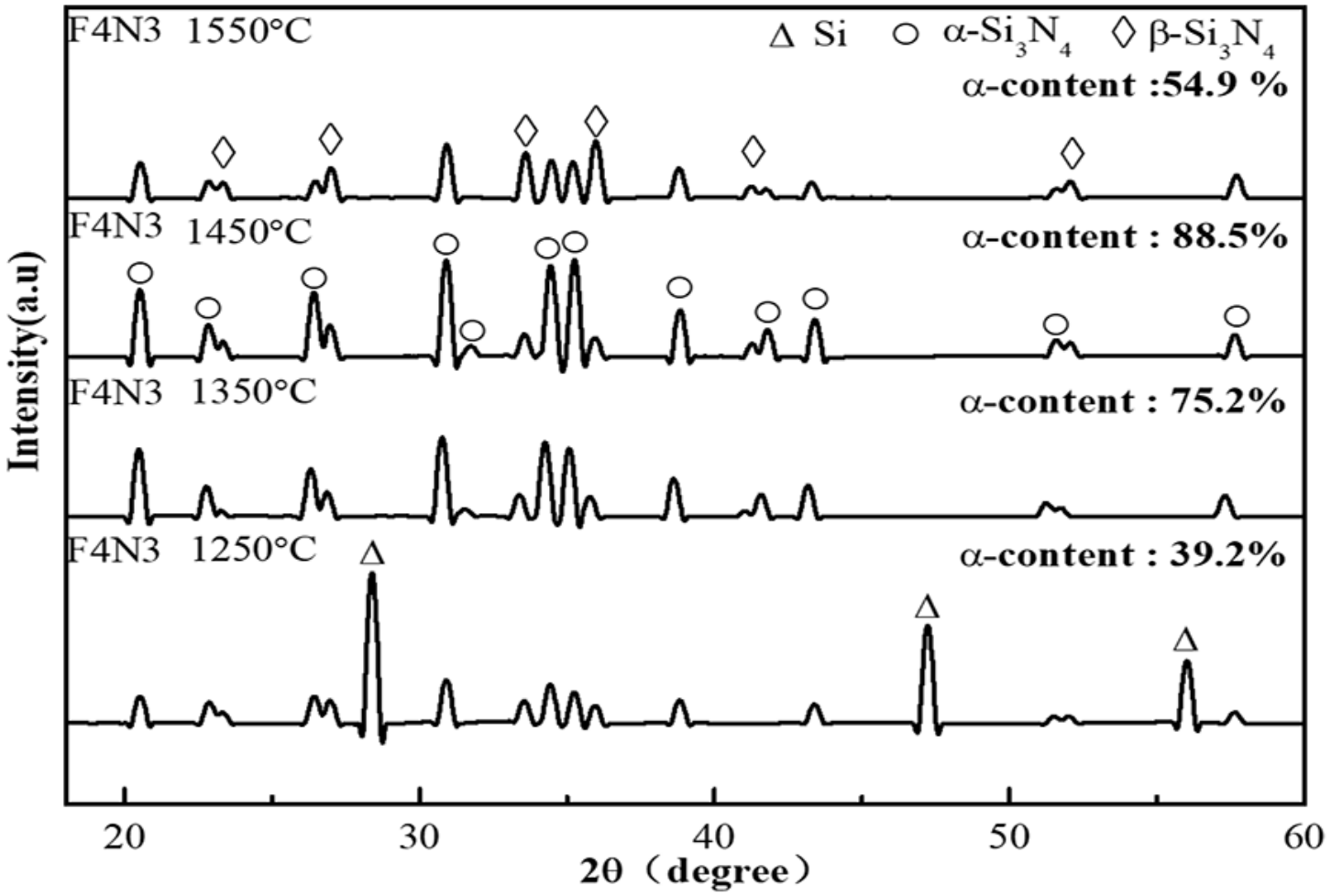

Figure 2

XRD patterns of the product synthesized for F4N3 sample at different temperatures, α content was estimated from the intensity of the respective XRD spectrum peak.

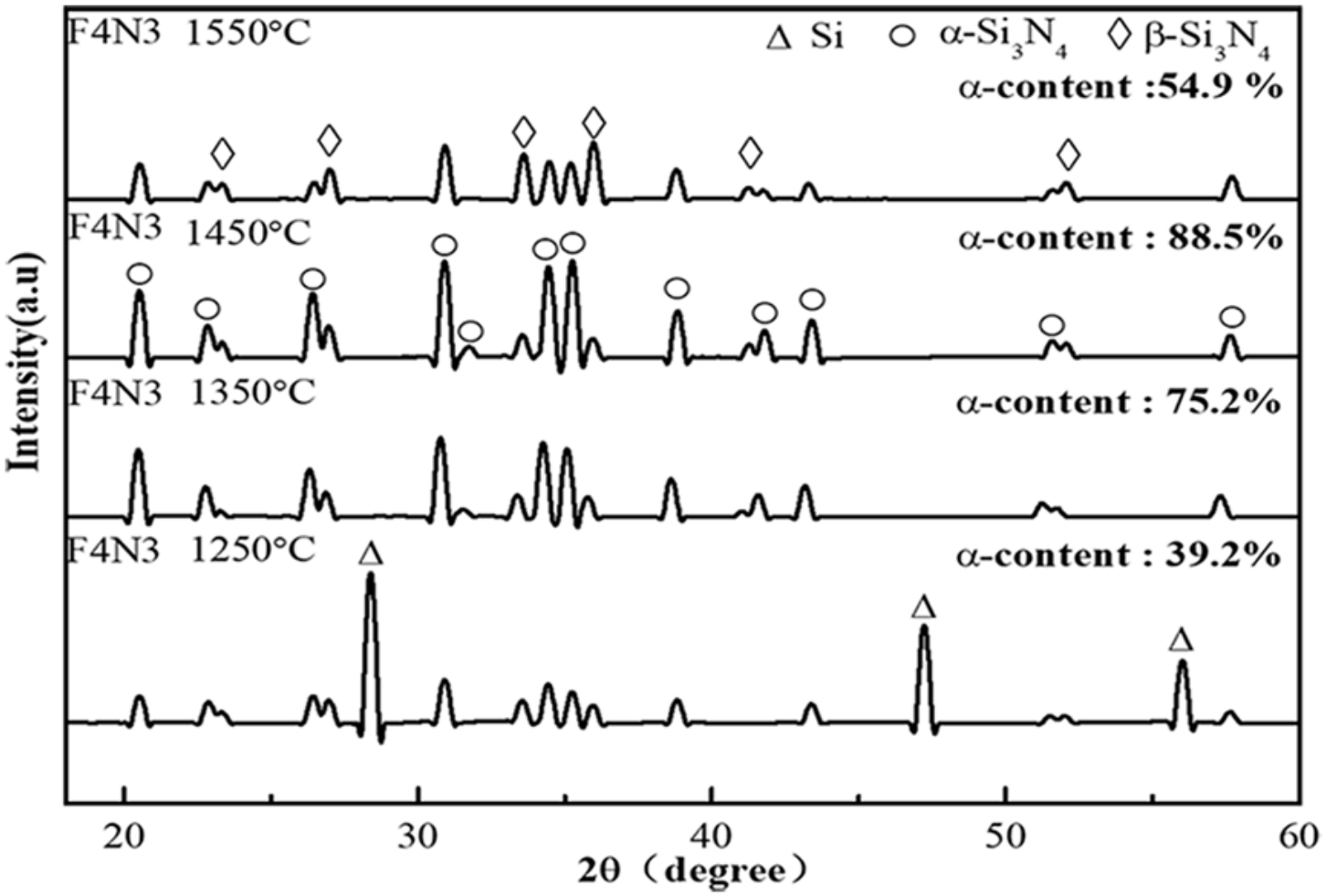

Figure 3

XRD patterns of the product synthesized for different Fe powder contents.

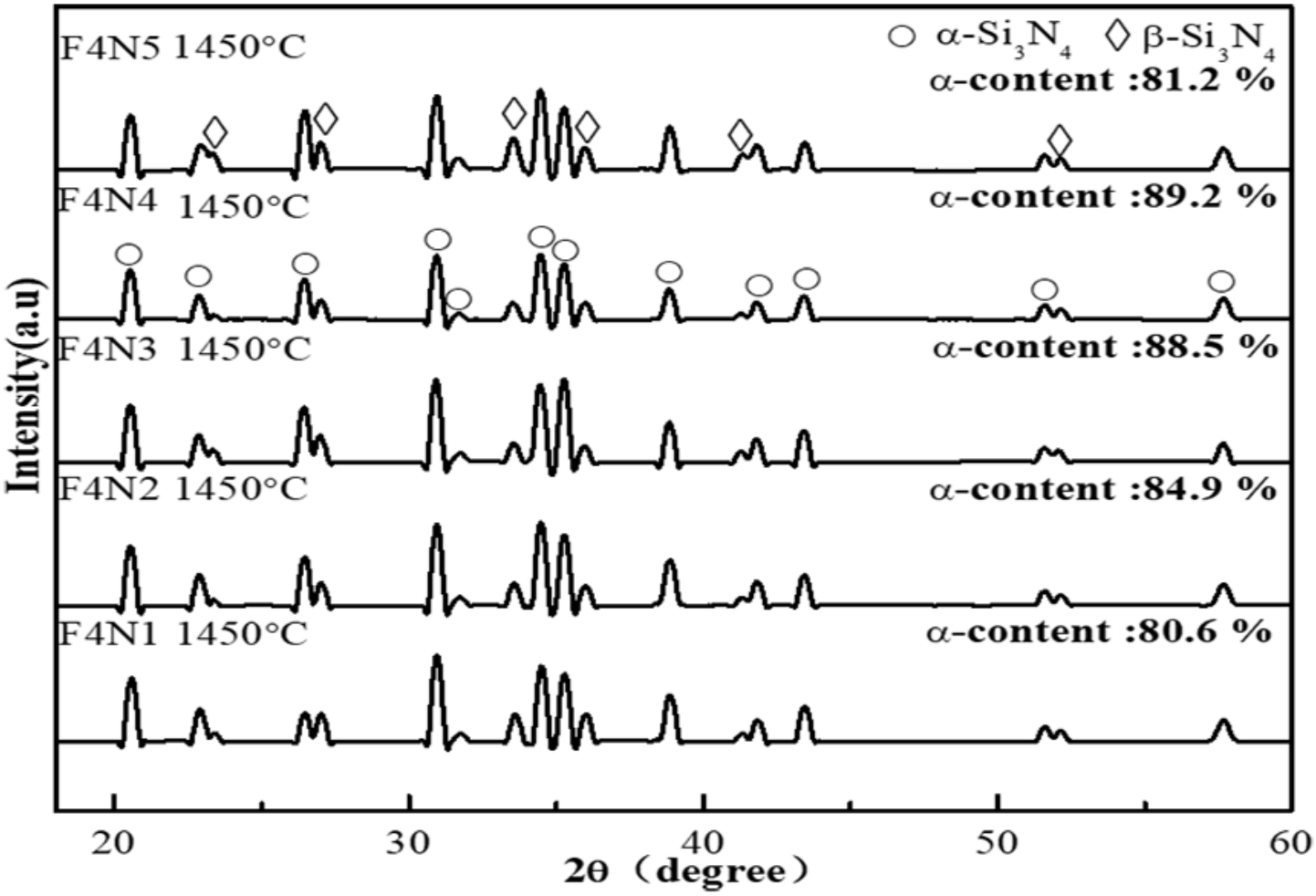

Figure 4

XRD patterns of the product synthesized with different NH4Cl contents.

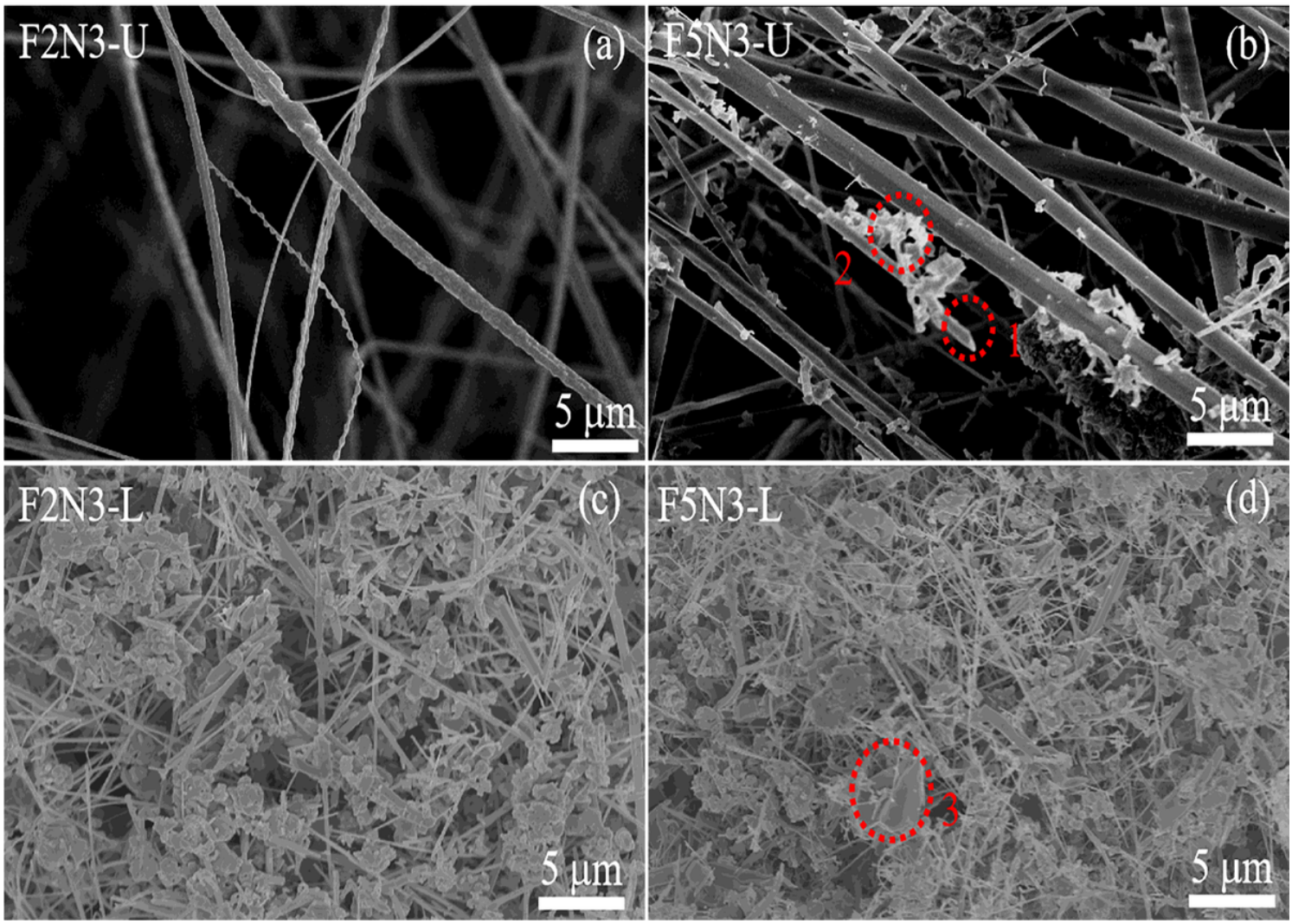

Figure 5

SEM images of the (a, b)upper (U) and (c, d)lower (L) layers of products synthesized from (a, c) F2N3 and (b, d) F5N3, in which several unique morphologies are produced such as seen in (b), number 1, thick nanowires with smooth surfaces, number 2, floating particles, and (d), number 3, blocky Si3N4.

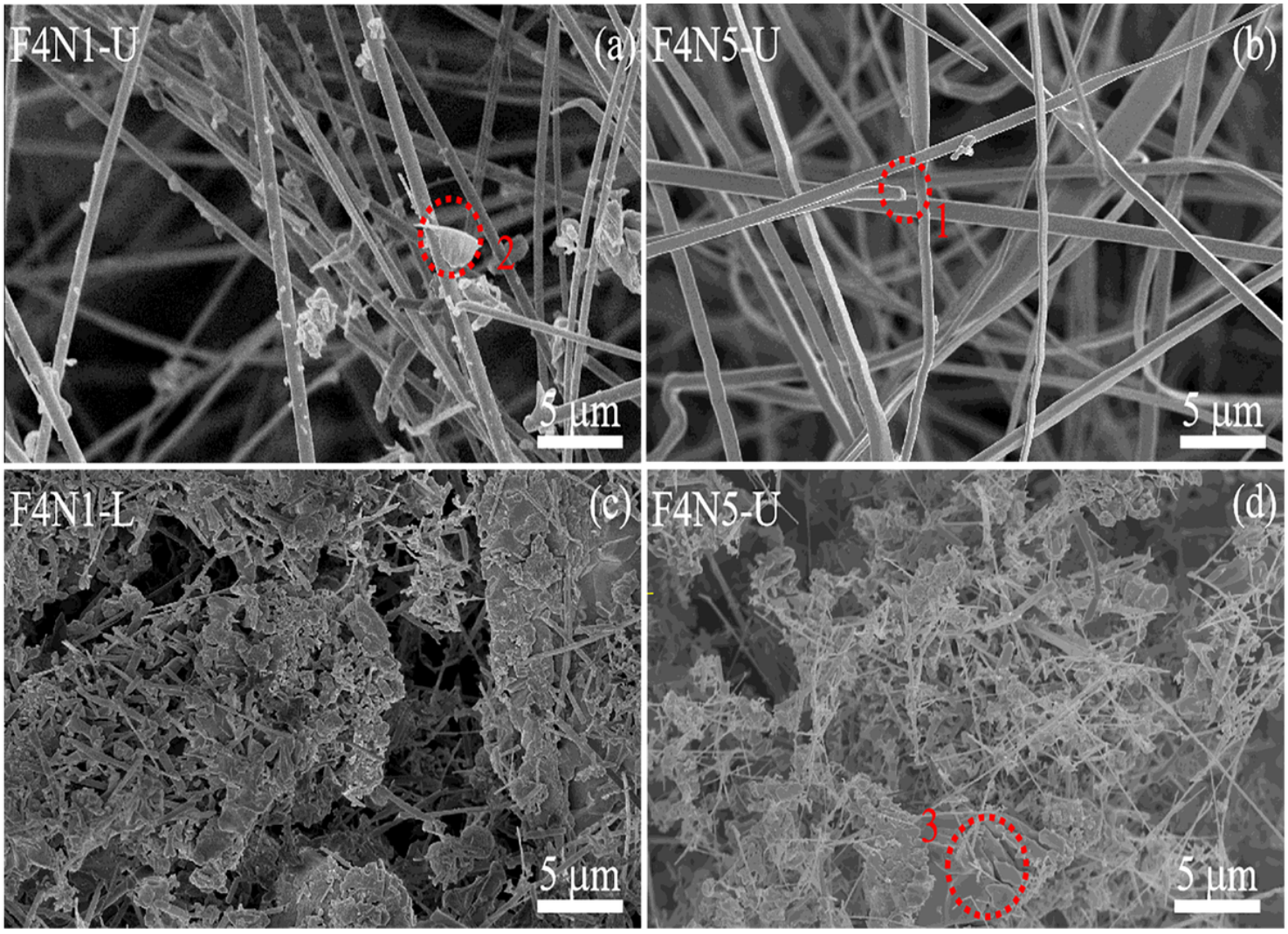

Figure 6

SEM images of the products synthesized the (a, b) upper (U) and (c, d) lower (L) layers for (a, c) F4N1 and (b, d) F4N5 samples. Figure 6 (a)2, (b) 1 and (d) 3 show the same structures as in Figure 5.

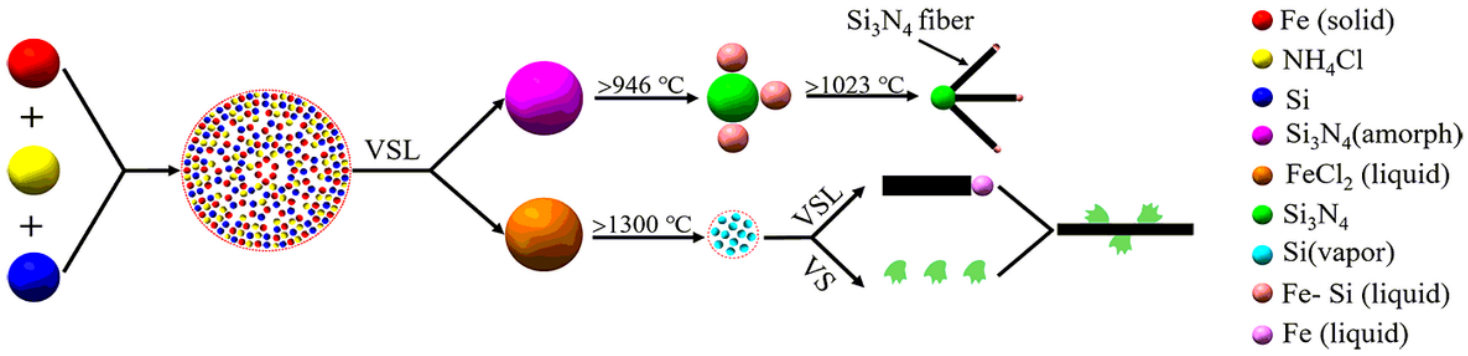

Figure 7

The simplified growth model of a Si3N4 fiber.